ADVANCED MATERIALS INTERFACES

www.advmatinterfaces.de

High Volumetric Quasi-Solid-State Sodium-Ion Capacitor under High Mass Loading Conditions

*Ranjith Thangavel, Aravindaraj G. Kannan, Rubha Ponraj, Myung-Soo Park, Hwan Choi, Dong-Won Kim, and Yun-Sung Lee**

The sodium-ion capacitor (NIC) represents an important research approach to bridge the gap between batteries and capacitors, but is still limited by inferior energy behavior at high power, low volumetric performance, low electrode mass loading, and safety issues with conventional liquid electrolyte. Herein, a high-performing, kinetically superior, and safer quasi-solid-state NIC utilizing the fast sodium storage in TiO_2 and rapid ion adsorption on a biomass-derived porous carbon with a sodium-ion conducting P(VDF-HFP) gel polymer electrolyte is presented. Owing to high mass loading, low graphene content in TiO_2, and by overcoming the diffusion-limited sodium storage by surface limited storage enable the NIC to deliver an impressive volumetric energy of ≈89 Wh L^{-1} (94 Wh kg^{-1}) based on total mass in both electrodes. Also, a remarkable power of ≈9.4 kW L^{-1} (10 kW kg^{-1}) while retaining an energy of ≈28.7 Wh L^{-1} (30.6 Wh kg^{-1}) is attained. Furthermore, the NIC shows a long-term stability both at room temperature and high temperature (50 °C), outperforming conventional NICs. This research opens new opportunities for applications of high-performing and safer NICs in next-generation storage devices requiring high energy at high power with high safety.

1. Introduction

Advancements in nanotechnology have broadened the market for electrical energy storage devices from small portable electronics to large electric vehicles.[1,2] Although primary research was focused on the development of high-energy lithium-ion batteries (LIBs), their insufficient power kinetics diverted the research focus toward the development of lithium-ion capacitors (LICs).[2,3] With a blend of high energy and high power, ion capacitors achieved a revolutionary advancement by bridging batteries and supercapacitors. Despite the commercial success and wide availability of LICs, limited availability of lithium resources raises questions on their future use in large-scale energy storage devices.[2,4]

Sodium-ion capacitors (NICs) are promising alternative devices owing to the wide availability of sodium resources and their competence for demonstrating higher performance than LICs.[5,6] NICs are fabricated by coupling a battery-type faradic electrode that stores sodium ions along with an electrical double-layer capacitor (EDLC)-type porous carbon electrode that stores anions simultaneously via quick surface adsorption.[7,8] NICs that exhibit enhanced energy retention at high power along with low energy loss per cycle is extensively under research.

To date, several NICs have been studied and demonstrated a remarkable gravimetric energy—power performance usually at low mass loading conditions. For practical applications, a high volumetric performance with high mass loading is crucial. But it faces several major challenges: (i) high active mass loading leads to poor electrolyte penetration deeper into thicker electrodes and thereby making causing severe ionic diffusion and electron transport losses, (ii) achieving a high stability and high rate performance at high mass loading conditions is difficult as a small morphology change could simulate electrode cracking or peeling from current collectors, (iii) very high amount of conductive carbon in battery-type electrode and carbon itself as battery-type electrode greatly decreases the volumetric performance.[9–13] Furthermore, safety issues related to liquid electrolyte inflammability, and leakage must be seriously addressed with an alternative.[14–19]

Battery electrodes in NICs primarily use intercalation-type compounds such as hard carbon, $NaTi_2(PO_4)_3$, $NiCo_2O_4$, $Na_2Fe_2(SO_4)_3$, and $Na_3Ti_2O_7$.[20–23] The sluggish diffusion-controlled sodium-ion storage in these compounds enables insertion of a limited number of sodium ions into the battery electrode at higher power and, lowers the energy output.[24–26] However, utilizing the strategy of sodium-ion storage on the surface of the battery electrode by quick surface pseudocapacitance is advantageous over diffusion-controlled bulk storage.[27–29] NICs driven by cationic surface pseudocapacitive intercalation could deliver superior energy, especially at high power, along with longer cycle life even under high mass loading conditions. The new approach could boost both the gravimetric and

R. Thangavel, H. Choi, Prof. Y.-S. Lee
Faculty of Applied Chemical Engineering
Chonnam National University
Gwangju 500757, Republic of Korea
E-mail: leeys@chonnam.ac.kr

Dr. A. G. Kannan, R. Ponraj, M.-S. Park, Prof. D.-W. Kim
Department of Chemical Engineering
Hanyang University
Seoul 04763, Republic of Korea

The ORCID identification number(s) for the author(s) of this article can be found under https://doi.org/10.1002/admi.201800472.

DOI: 10.1002/admi.201800472

volumetric energy output at high power in NICs, establishing a real trade-off relationship between batteries and capacitors.

Only a few among several battery electrodes exhibit surface pseudocapacitive sodium-ion storage.[30–32] Among them, electrochemically active anatase TiO_2 demonstrates a dominating pseudocapacitive behavior even at high current owing to its 3D favorable interstitial sites for sodium-ion accommodation and excellent structural stability.[33–35] Aside from its abundance and low cost, its superior environmental friendliness make TiO_2 an excellent material for commercial energy storage devices. Improving the poor intrinsic electrical conductivity of TiO_2 is crucial to overcome kinetic limitations and expand its maximum output capability. Strategies such as downsizing the particles to a nanomorphology and carbon-coating techniques (using CNTs and graphene) have been developed to enhance its output performance.[36,37] However, the conductive carbon network should be maintained as low as possible to ensure the high electrode packing density. However, to date a huge amount of conductive carbon is used that severely downgrades the volumetric performance.

Meanwhile, the capacitor-type porous carbon electrode must work efficiently to establish a kinetic balance in the NIC system by adsorbing equivalent anions, thereby maintaining equilibrium.[38,39] The poor adsorption kinetics of commercial microporous activated carbon (ACs), and sluggish ion accessibility into their inner micropores due to limited transport kinetics downgrades their performance at higher power and high mass loading.[40,41] Further, porous carbon derived from coke and petroleum raises concern over their environmental friendliness.[42] In the search for an efficient capacitor-type electrode, porous carbons derived from biowaste can be capable alternatives in NICs. Tailored biomass-derived carbon with a highly porous 3D network along with a large number of mesopores enhances kinetics inside the pores by several orders, providing maximized adsorption ability.[43–46]

Herein, we present a new quasi-solid-state sodium-ion capacitor by coupling the kinetically superior pseudocapacitive TiO_2 battery electrode and porous carbon derived from waste watermelon rind (RDC) capacitor electrode in sodium-ion-conducting gel polymer electrolyte P(VDF-HFP) matrix that can function efficiently under high mass loading conditions. The current device has a great advantage of exceptionally high volumetric energy—power, high temperature adaptability, high coulombic efficiency, and a superior stability. The configured NIC outperforms the NICs fabricated with conventional liquid electrolytes and thereby bridging the performance gap between the batteries and capacitors.

2. Characterization

2.1. Physical Characterization

Morphological features of all samples were recorded by scanning electron microscopy (SEM; S4700, Hitachi, Japan) and high-resolution transmission electron microscopy (HRTEM; TecnaiF20, Philips, Holland). X-ray diffraction (XRD) patterns were recorded on a Rigaku Rint 1000 (Japan) with a CuKα radiation source. The diffraction patterns are collected between 10° and 80° at a scan rate of 4° min^{-1} keeping the tube voltage at 40 kV and tube current at 40 mA. X-ray photoelectron spectroscopy (XPS) performed using a VG Multilab ESCA System 220i Spectrometer, equipped with an AlKα X-ray source ($h\nu$ = 1486.6 eV). XPS was carried out at a photoelectron take-off angle of 90° to the sample surface. The charge correction was performed by fixing the hydrocarbon component of the C 1s peak to 284.6 eV. Raman spectra were obtained using a Lab Ram HR 800 Raman dispersive spectrometer (Horiba, Japan). Nitrogen adsorption and desorption isotherm measurements were performed on Micromeritics, USA analyzer at 77 K. ASAP 2020 (version 4.02) was used to calculate the Brunauer–Emmett–Teller (BET) surface area and pore volume. The thermogravimetric (TG) analysis was performed using a thermal analyzer system (STA 1640, Stanton Redcroft Inc., UK) at a scan rate of 5 °C min^{-1}, in ambient air.

2.2. Electrochemical Characterization

The working electrodes were formulated with active material (75 wt%), carbon black (15 wt%) as conductive carbon, and Teflonized acetylene black binder (10 wt%). The electrode slurry was cast and pressured over a stainless-steel mesh and then dried at 160 °C for 4 h in a vacuum oven, and the diameter of the working electrode is 1 cm. For half-cell testing, the sodium metal was used as counter electrode against the working electrode (reduced graphene oxide (rGO)-TiO_2 or RDC). The working potential window for TiO_2 anode, and RDC cathode were between 0.05 and 3 V and 1.5 and 4.5 V, respectively. For hybrid capacitor testing, two asymmetric electrodes (rGO-TiO_2: RDC) were assembled inside a CR 2032 coin cell in a dry argon-filled glove box. Prior to NIC assembly, rGO-TiO_2 electrodes were galvanostatically cycled for few times against sodium metal in half-cell. And then the electrodes were removed and assembled into NIC against RDC electrode. The electrodes were separated with a P(VDF-HFP) gel polymer electrolyte. The P(VDF-HFP) white membrane was soaked in $NaClO_4$ in ethylene carbonate (EC)/dimethyl carbonate (DMC) electrolyte for 12 h in a glove box to obtain a gel polymer electrolyte. The as-fabricated NICs were tested between 1 and 4 V. Cyclic voltammetry (CV) and electrochemical impedance spectroscopy (EIS) were analyzed with a Bio-Logic electrochemical workstation (SP-150), France, and a Won-A-Tech Battery tester (WBCS 3000, Korea) was used for galvanostatic charge–discharge studies. The power density is calculated as $P = (I\ V/2m)$ kW kg^{-1}, where I is the current density, V is the working potential of the system, and m is the mass in both electrodes. The energy density is calculated as $E = (P \times t)$ Wh kg^{-1}, where t is the discharge time. Volumetric calculations are based on thickness of electrodes over the current collector. The density of rGO-TiO_2 and RDC electrodes were ≈ 2.1 and 0.56 g cc^{-1}, respectively.

3. Results and Discussion

SEM images of rGO-TiO_2 (Figure S1a,b, Supporting Information) reveal dense and uniform growth of nanostructured TiO_2 particles on the graphene sheets. TEM images of rGO-TiO_2

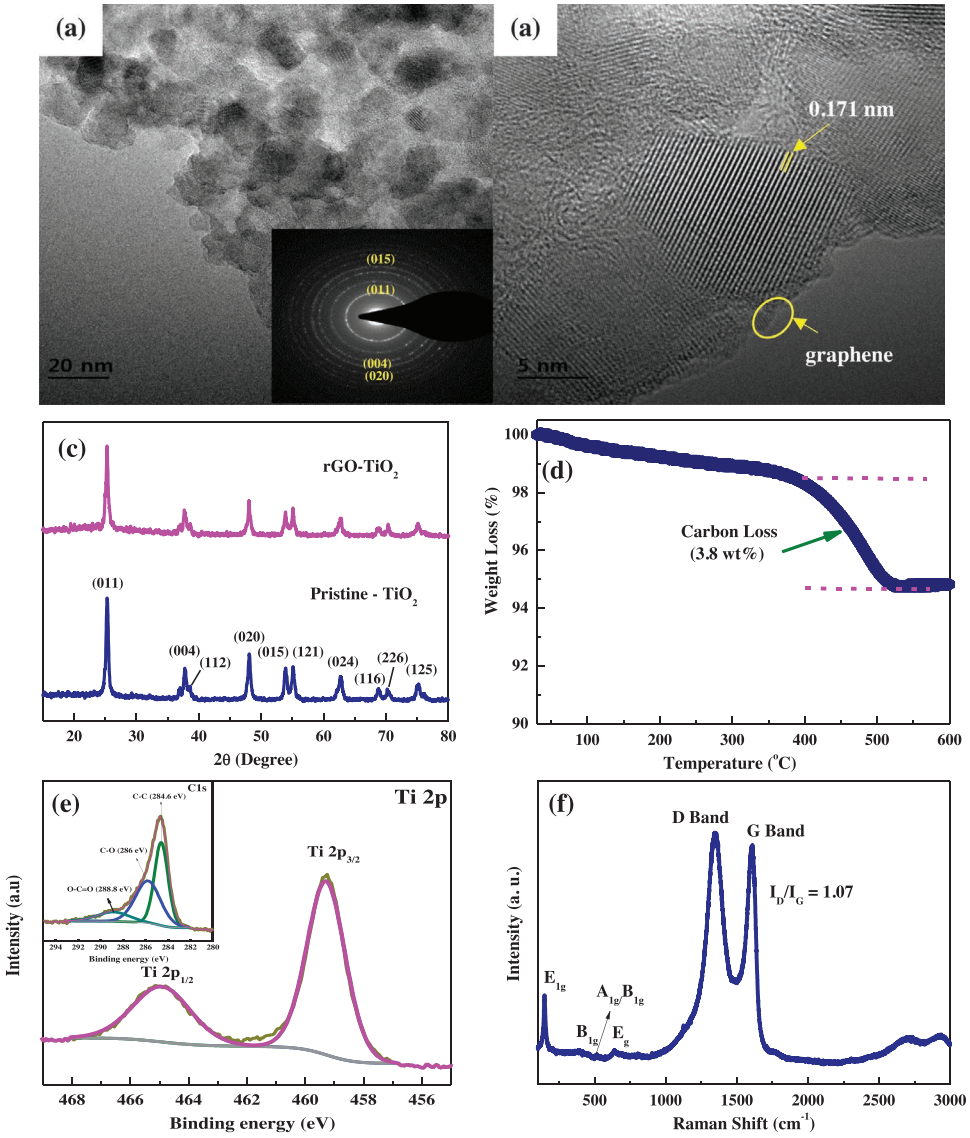

Figure 1. a) TEM image of rGO-TiO_2, b) HR-TEM image of rGO-TiO_2, c) XRD patterns of TiO_2 and rGO-TiO_2, d) TG analysis spectrum of rGO-TiO_2, e) deconvoluted Ti2p XPS survey spectrum of rGO-TiO_2 (inset: deconvoluted C1s spectrum), and f) Raman spectrum of rGO-TiO_2.

(**Figure 1**a, and Figure S1c,d, Supporting Information) confirm the uniform and dense growth of nanosized TiO_2 particles on the graphene surface and the size of TiO_2 particles are in the range of ≈8–10 nm. It can be clearly seen that TiO_2 particles are connected by graphene bridges and no free TiO_2 particles are visible. The corresponding selected area diffraction (SAED) pattern shows well-defined concentric rings, which indicates that the formed TiO_2 particles are polycrystalline in nature. The HR-TEM image (Figure 1b) displays the lattice spacing of 0.171 nm, corresponding to the (015) plane of anatase-type TiO_2, and confirming its highly crystalline nature.[47–49] Furthermore, the HRTEM image confirms the highly folded sheet-like morphology of graphene sheets, along with the highly exfoliated graphene. From an rGO folded area (indicated by yellow circle) we can observe predominantly less than ten layers of graphene sheets. The hybrid design of growing the nano-TiO_2 sandwiched between graphene bridges is highly favorable for enhancing the Na-ion kinetics and electronic conductivity between TiO_2 particles.[50,51] XRD patterns of the pristine TiO_2 and rGO-TiO_2 in Figure 1c exhibit well-defined crystalline peaks, indexed to anatase-type TiO_2 (JCPDS Data No. 22-1272). The weight percentage of graphene in the rGO-TiO_2 hybrid is calculated to be ≈3.50% by TG analysis graph. The weight loss at 400–600 °C in Figure 1d corresponds to the combustion of graphene in air during TG analysis. The presence of a low quantity of graphene sheets did not affect the crystallinity of the particles. The low graphene content is enough to anchor all TiO_2 particles due to their large dimensions and this greatly improves the volumetric performance of the electrode.[52,53]

The chemical nature of rGO-TiO_2 hybrid was analyzed through the XPS spectrum given in Figure S2 (Supporting Information). The XPS survey spectrum confirms the presence of C, O, and Ti.[41] The deconvoluted C 1s spectrum (Figure 1e) shows a broad peak at ≈284.6 due to sp^2 C—C binding energy

along with surface functionalities at 288.8 eV (O—C=O) and 285.9 eV (C—O). The presence of oxygen functional groups indicates that residual oxygen functionalities remain even after reducing at 600 °C in Ar atmosphere. The deconvoluted Ti 2p spectrum shows two peaks at ≈465 and ≈459 eV, confirming the tetravalent state of titanium in TiO_2.[25] The Raman spectrum of rGO-TiO_2 is presented in Figure 1f. The strong bands at ≈149 and 639 cm^{-1} correspond to E_{1g} mode vibrations and the bands at 399 and 516 cm^{-1} correspond to A_{1g} mode and B_{1g} mode vibrations of anatase-type TiO_2, respectively.[47] The presence of graphene is further evidenced from two broad-bands at ≈1365 and ≈1610 cm^{-1}, assigned to the D and G bands, respectively. Additionally, a small peak at ≈2700 cm^{-1} was detected corresponding to the 2D band of reduced graphene and indicating the predominant presence of few-layered graphene sheets. The I_D/I_G ratio of rGO-TiO_2 gives a high value of ≈1.08 due to the highly reduced and defective nature of reduced graphene oxide (GO) sheets.[54]

The N_2 adsorption–desorption isotherm of rGO-TiO_2 in Figure S3 (Supporting Information) exhibits a Type IV isotherm, revealing the presence of a large number of mesopores in the hybrid. The BET surface area was analyzed to be ≈98 m^2 g^{-1}, which favorably provides a large number of active surface sites for sodium-ion storage. Furthermore, the large number of mesopore channels aids fast sodium-ion migration by providing a shortened ionic path.[55–57]

The XRD pattern of the synthesized porous carbon (Figure S4a, Supporting Information) shows a highly amorphous nature with strong and broad peaks around 2θ = 25° and 43°, corresponding to the (002) and (001) graphitic planes. SEM images of RDC in Figure S4b (Supporting Information) primarily consist of irregular spherical particles in the dimension of few micrometers with randomly distributed pores all over the surface, originating from KOH activation. HR-TEM images in **Figure 2**a,b confirm the randomly distributed micro- and mesopores over the carbon surface with no graphitic ribbons. The Raman spectrum of RDC given in Figure 2c shows a strong G band at ≈1580 cm^{-1} and D band at ≈1350 cm^{-1}, corresponding to in-plane graphitic vibrations and double resonance from disordered carbons, respectively. The I_D/I_G value was calculated to be ≈0.97; such a high value is attributed to defects and disorder in RDC. The chemical nature of RDC is analyzed by XPS analysis and the XPS survey spectrum in Figure 2d shows the presence of carbon and oxygen along with nitrogen heteroatoms. The deconvoluted C1s spectrum in Figure 2e shows the sp2 hybridized carbon at ≈284.6 eV along with oxygen functionalities. The deconvoluted N1s spectrum in Figure 2f shows the presence of pyridinic, pyrrolic, and quaternary type of nitrogen on carbon framework. Such type of nitrogen heteroatoms can greatly enhance the electrical conductivity of porous carbon and helps to achieve a high rate performance.[58]

The N_2 adsorption–desorption of RDC shown in Figure S5 (Supporting Information) exhibits a Type IV isotherm with significant slope at low partial pressure and a hysteresis loop in the high partial pressure region. This is attributed to capillary condensation of adsorbed nitrogen in small mesopores and the BET specific surface area of RDC was measured to be ≈2344 m^2 g^{-1}. The higher surface area of RDC is likely to originate from multiple defects and holes formation over individual graphene sheets in RDC in the high temperature activation condition with large concentration of KOH.[59] These characteristics favorably increase the active sites for ionic adsorption. The Barrett–Joyner–Halenda (BJH) pore distribution (inset, Figure S5, Supporting Information) reveals virtually no pores larger than 5 nm and is in agreement with TEM images and the mean pore diameter of RDC was observed to be ≈2.7 nm. The presence of a large number of small mesopores along with micropores is key to achieving high adsorption even at a high current rate.[60,61] The meso-micro pore hierarchical architecture provides channels for ionic movement, reducing the ion travel distance to deeper micropores and reducing the resistance to ion adsorption.

3.1. Half-Cell Performance

The sodium-ion storage of rGO-TiO_2 and pristine TiO_2 was investigated through galvanostatic charge–discharge (CD) studies between 0.05 and 3 V. The initial charge–discharge graph of pristine TiO_2 and rGO-TiO_2 in Figure S6a (Supporting Information) shows the coulombic efficiency of ≈14.8 and 19.25%, respectively. The large irreversible capacity loss arise from solid electrolyte interphase (SEI) layer due to the electrolyte decomposition during the first cycle. This is a common phenomenon observed for anode materials and can be improved by electrolyte optimization, conductive carbon, and binder in the electrode. However, within few cycles the coulombic efficiency increases and reached near ≈99%. The CD curves of both samples in **Figure 3**a and Figure S6b (Supporting Information) exhibit a broad sloppy shape profile with no plateaus and agree with previous reports. Despite various ion storage mechanisms for TiO_2 being proposed to date, the major capacity contribution is from a combination of pseudocapacitive surface sodium-ion adsorption at higher potential and sodium intercalation at lower potential.[48] The discharge capacities at different rGO-TiO_2 mass loading conditions are shown in Figure 3b. At rGO-TiO_2 loading of 1 mg cm^{-2}, the discharge capacities of ≈248, 171, 137, 120, and 110 mAh g^{-1} at 0.25, 1, 2.5, 5, and 10 C (1 C = 0.33 A g^{-1}) are achieved. With increase in mass loading the discharge capacity decreases due to increase in electrode thickness. Even at a high mass loading of ≈5 mg cm^{-2}, rGO-TiO_2 can perform efficiently and high discharge capacities of ≈204, 149, 110, 76, and 55 mAh g^{-1} are obtained at 0.25, 1, 2.5, 5, and 10 C, respectively. In contrast, the discharge capacity of pristine TiO_2 is significantly lower than rGO-TiO_2 at all rates (Figure S6a, Supporting Information). Pristine TiO_2 delivered a poor discharge capacity of ≈138, 108, 75, 30, and 12 mAh g^{-1} at 0.25, 1, 2.5, 5, and 10 C, respectively. The poor rate capacity and failure of pristine TiO_2 at higher current are due to poor electronic conductivity between TiO_2 particles that impedes Na-ion kinetics. The highly conductive rGO network interconnecting the TiO_2 particles enhances Na-ion kinetics thereby aiding to achieve high capacity even at high current rate. Even when the current density was returned to low current rate from a higher current, rGO-TiO_2 delivered almost the same capacity with no capacity fading. Meanwhile, pristine TiO_2 cannot retain its initial capacity, showing a large capacity loss. This depicts that rate performance and sodium-ion reversibility of TiO_2

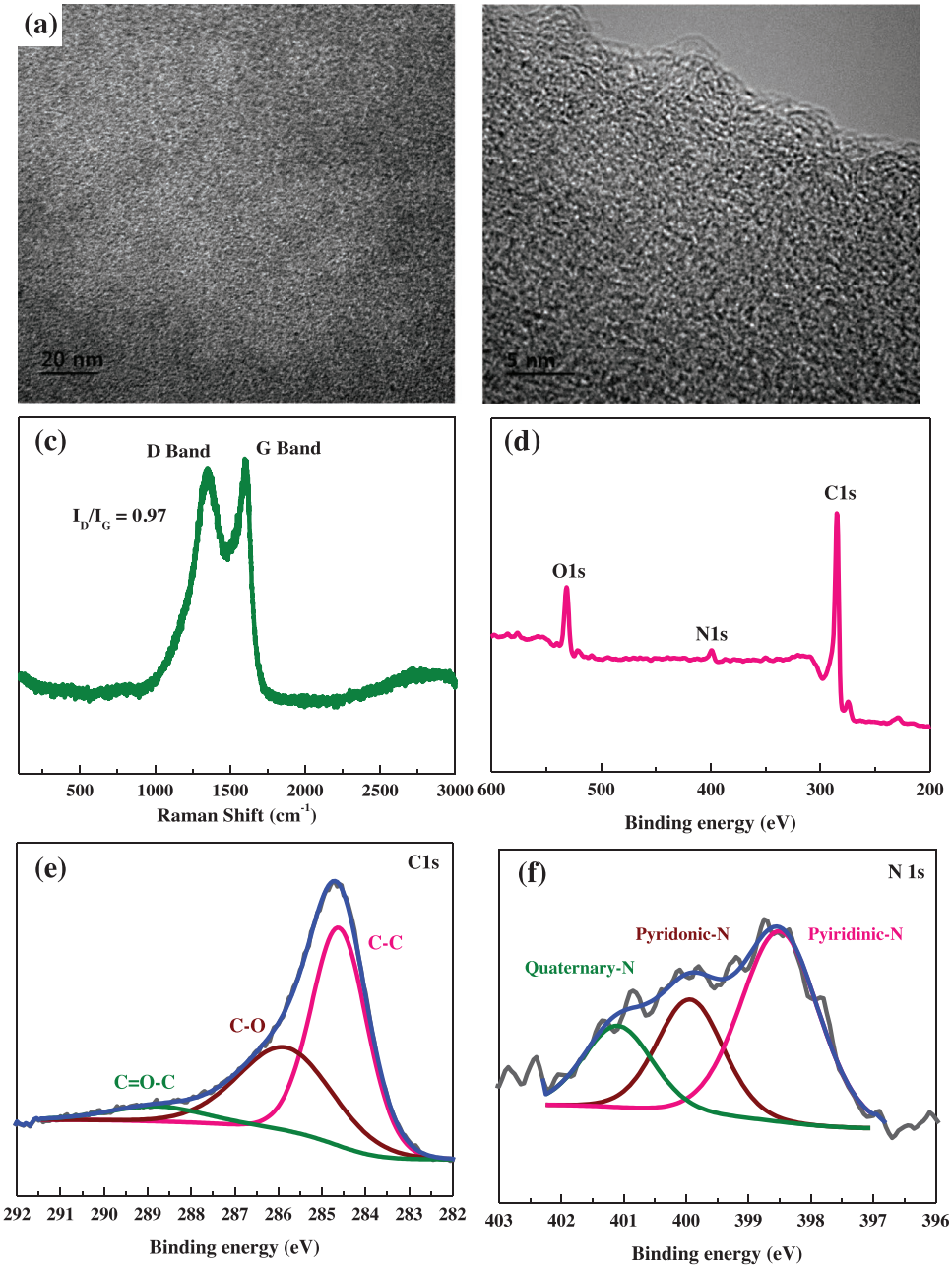

Figure 2. a,b) TEM images of RDC, c) Raman spectrum of RDC, d) XPS survey spectrum of RDC, e) deconvoluted C1s spectrum, and f) deconvoluted N1s spectrum.

have been enhanced by several orders by the highly conductive and porous rGO matrix and by the smaller TiO_2 particles. This is further verified by EIS studies, the Nyquist plot in Figure S6c (Supporting Information), where the reduction in charge transfer resistance is noted after the incorporation of conductive graphene network. The highly mesoporous nature of rGO-TiO_2 plays an important role in providing an easier and shorter sodium-ion diffusion path from electrolyte to TiO_2 particle even under high mass loading conditions.[35,49]

To elucidate the Na-ion storage properties of rGO-TiO_2, cyclic voltammetry was performed against Na metal between 0.05 and 3 V at different scan rates (Figure 3d). The cyclic voltammograms of rGO-TiO_2 show a broad rectangular profile with redox peaks at ≈0.5 and ≈0.8 V due to sodium insertion/extraction, respectively. With increasing scan rate, the shape profile is maintained and the output currents are directly proportional to sweep rates and thereby follow the power law $i = av^b$, where i is the current (A), a and b are the adjustable parameters, and v is the scan rate (mV s^{-1}).[55,62] From the CV curves, b is calculated to be ≈0.98, demonstrating that Na-ion storage in rGO-TiO_2 occurs through a fast surface-controlled redox reaction. ≈80% of the total capacity is identified to be from pseudocapacitive reaction at 1 mV s^{-1} (Figure 3e). The fast surface-limited Na-ion storage characteristic of rGO-TiO_2 is

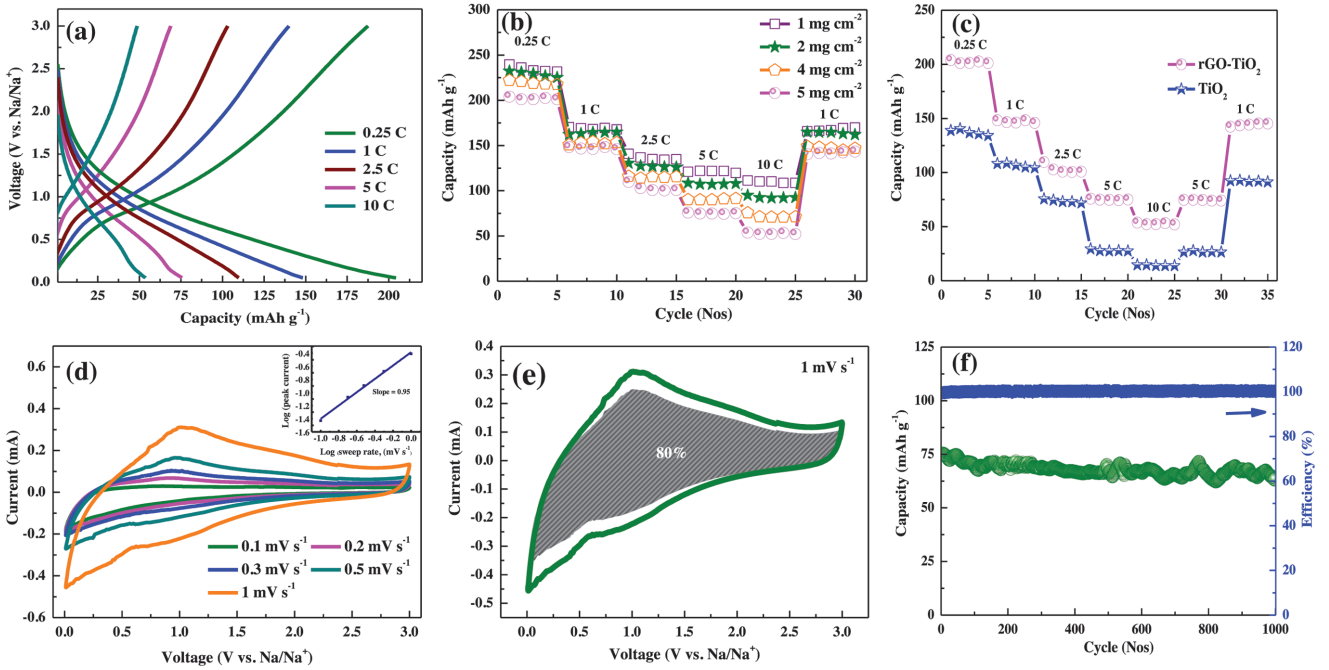

Figure 3. a) Charge/discharge profile of rGO-TiO_2 at different current rates, b) rate performance of rGO-TiO_2 at different mass loading, c) rate performance of rGO-TiO_2 and pristine TiO_2, d) cyclic voltammetry curves of rGO-TiO_2 at various scan rates (inset: relationship between cathodic current and scan rate), e) capacitive contribution and diffusion contribution of rGO-TiO_2 at 1 mV s^{-1}, and f) cycling stability of rGO-TiO_2.

highly favorable for achieving a high capacity at high current rates even under high mass loading conditions and thereby enables a possibility of high volumetric and high-power NICs.[55,62] The previously studied insertion compounds exhibit diffusion-controlled reactions that unfavorably restrict the working of NICs at high power rates.[20]

The cyclability of TiO_2 and rGO-TiO_2 (5 mg cm^{-2}) is given in Figure S6d (Supporting Information) and Figure 3f, respectively. Pristine TiO_2 demonstrated inferior cyclability even at a low current rate retaining ≈60% initial capacity after 100 cycles. However, rGO-TiO_2 demonstrated excellent cyclability after 1000 cycles at 5 C, depicting its strong reversibility and structural stability against repeated sodium-ion storage despite the high current and high mass conditions. More interestingly, regardless of the low coulombic efficiency during initial cycles, high coulombic efficiency of ≈99% was achieved in the next few cycles and was maintained throughout. Such a high stability even with high loading is essential to design a stable sodium-ion capacitor system. The results indicate a low quantity of enough to accommodate all nano TiO_2 regime and overcome any volume changes on repeated sodiation/desodiation.

Volumetric and aerial capacities are more important to achieve high energy at a limited space and the calculated volumetric and aerial capacity of rGO-TiO_2 are given in Figure S7 (Supporting Information). The rGO-TiO_2 shows a volumetric capacity of ≈429 mAh cc^{-1} and an areal capacity of ≈1.06 mAh cm^{-2} at 0.25 C. A high capacity has been retained by rGO-TiO_2 even under a high mass loading (5 mg cm^{-2}), making a favorable condition to achieve a high volumetric energy. The previous reports on NICs generally utilize a low mass loading (1–1.5 mg cm^{-2}) to achieve a high capacity, and the mass loading in the present study is 3–5 orders higher than the previous reports.[55,63]

The electrochemical performance of RDC is analyzed in a half-cell configuration against Na metal at 1.5–4.5 V, which will be employed as an adsorption electrode for NIC. The CV curves in Figure S8a (Supporting Information) show a broad rectangular box-like shape, indicating a surface anion storage in RDC. Additionally, a linear increase in current with scan rate is observed (Figure S8b, Supporting Information), indicating a capacitive-type reaction in RDC. On positive polarization RDC reversibly adsorb ClO_4 anion and release Na cations. However, on negative polarization the rectangular shape curve is slightly distorted near 1.7 V due to limited accessibility of cations into pores. However, these are less pronounced for Na^+-based system than Li^+ systems.[7,57] However, the NIC cells do not allow the capacitive-type RDC electrodes to reach the ion-sieving potential since the potential swing of the negative battery-type TiO_2 electrode always keeps the RDC electrode above those potentials, avoiding cation-sieving to become a limiting factor for the NIC at fast working condition.[58] The CD curves of RDC in **Figure 4**a and Figure S8c (Supporting Information) exhibited relatively straight and flat profile due to the reversible adsorption/desorption of ClO_4 anions over the pores of the carbon. RDC delivered a high capacity of ≈175 mAh g^{-1} at 1 A g^{-1} and the majority of capacity obtained is through double-layer formation of ClO_4 anion. The high capacity was achieved due to synergistic effect of the presence of a large number of pore in a wide operating potential window. The maximized window can easily facilitate the utilization of large number for pores in RDC for adsorption reactions. The electrolyte is much stable under the operating potential and electrolyte decomposition is not observed from the CV curves.[7] Additionally, a very slight pseudocapacitance due to sodium-ion interaction with oxygen functionalities is also noted. However,

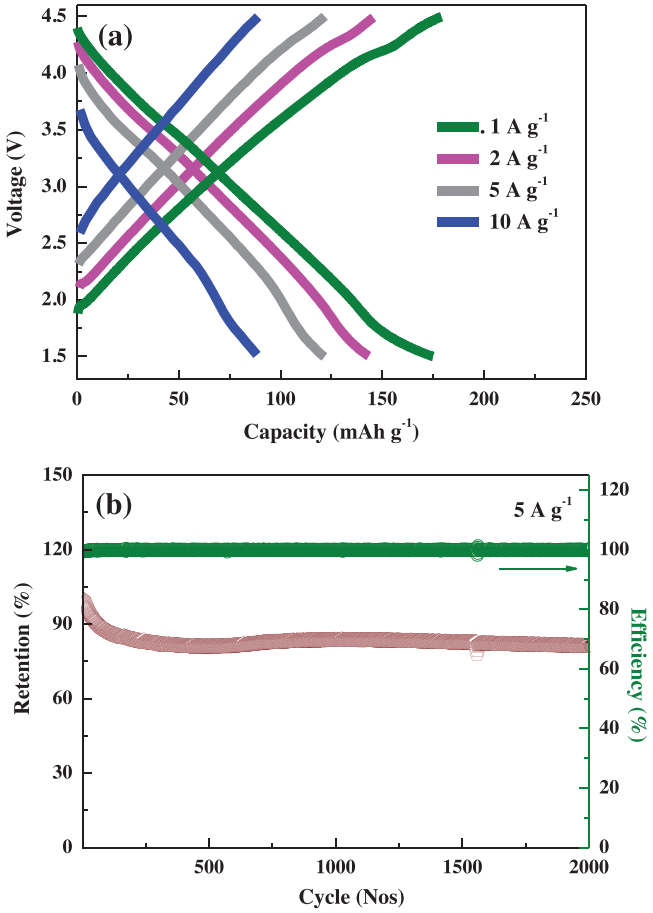

Figure 4. a) Charge/discharge curves of RDC, and b) cycling stability of RDC.

the pseudocapacitance reaction is reversible and has been discussed in previous studies.[7,19] Even with an increase in current density, the CD curves maintained their shape profile without any distortion. At 10 A g^{-1} RDC delivered a high capacitance of ≈88 mAh g^{-1} while conventional activated carbon and other porous carbon failed to work. Electrodes with a mass loading of ≈5 mg cm^{-2} also showed a high performance, retaining ≈80% of capacity at 10 A g^{-1} even when the mass is increased by five times. A capacity of ≈74 mAh g^{-1} has been delivered at 10 A g^{-1} with the mass loading of ≈5 mg cm^{-2} (Figure S8d, Supporting Information). Table S1 (Supporting Information) compares the capacity delivered by some previously reported porous carbon and the superiority of the RDC can be clearly noted. The high capacity values evidence the enhanced adsorption kinetics of RDC with its highly mesoporous 3D hierarchical architecture and large pore volume. The wider and smoother mesopore channels of RDC facilitate easier and quicker electrolyte flow into deeper pores, making them readily available for ionic adsorption even at higher current rates.[64,65] The hierarchical architecture can enable the participation of the innermost pore toward ion adsorption reactions. The cycling stability of RDC was tested at 5 A g^{-1} and the results are shown in Figure 4b. After capacity stability within a few cycles, a high capacity is retained even after 2000 cycles. The RDC showed a capacity retention of ≈87% after 100th cycle and then well stabilized, retaining ≈84% of initial capacity even after 2000th cycle. RDC delivered remarkable stability performance at high mass loading condition, outperforming previously reported adsorption electrodes and thereby qualifying to serve in long-term energy storage devices.

3.2. Sodium-Ion Capacitor

Sodium-ion capacitors were tested in the extended voltage window of 1–4 V with rGO-TiO_2 and RDC electrodes separated by a P(VDF-HFP) polymer electrolyte. Utilizing such novel gel polymer electrolyte with conductivity equivalent to conventional liquid electrolyte can greatly elevate the safety of the NICs while retaining the performance of the system.[17] It is also worth to note here that such a high-voltage NICs could offer a high output energy.[39,66,67] The optimized mass ratio between anode and cathode is found to be 1:1 (the detailed information is shown in Figure S9, Supporting Information).

The CV curves of the NIC are given in **Figure 5**a and show a broad asymmetric shape profile, deviating from the linear rectangular shape profile as exhibited by EDLCs implying pseudocapacitive sodium -ion storage in NIC along with non-faradaic adsorption.[68,69] Overcoming the diffusion-limited sodium-ion storage by new surface-limited ion storage can greatly increase the energy retention at higher power. Furthermore, the shape profiles of the CV curves are maintained even at high scan rate showing that NIC retain its activity at high rate.[16] The CD curves in Figure 5b shows the presence typical capacitive behavior in NIC cell due to the presence of a double capacitive charge storage mechanism in NIC. The working mechanism of NIC is as follows: (i) during the charging process, sodium ions from the electrolyte undergo reversible surface pseudocapacitive storage over rGO-TiO_2 along with simultaneous ClO_4 anionic double -layer capacitive adsorption over RDC to form a double layer, and (ii) reversal of the above reactions occurs during the discharge process.[15,70–72] Even at high current rates, the shape profile of CD curves was maintained, indicating the smooth and facile storage reactions in NIC at high power.

From the CD curves, the energy and power densities were calculated based only on the active mass in both electrodes and presented in a Ragone plot (Figure 5c). It can be seen that the quasi–solid-state NIC can deliver a very high energy of ≈123.4 Wh kg^{-1} at 0.125 kW kg^{-1}. Even at the ultrahigh power of ≈12.5 kW kg^{-1}, NIC can retain the energy density of ≈38.2 Wh kg^{-1}. The energy and power behavior are equivalent to performance of NICs obtained with conventional liquid electrolytes. The Ragone plots clearly show a superior energy output and energy retention at such power exceeds the conventional NICs with diffusion-controlled energy storage. This current NIC has outperformed lithium hybrid capacitors and other NICs constructed with metal oxides such as V_2O_5, Nb_2O_5, $NiCo_2O_4$, and diffusion-controlled intercalation compounds such as hard carbon, $Na_3V_2(PO_4)_3$, $Li_4Ti_5O_{12}$, $NaTi_2(PO_4)_3$, and $NaTi_3O_7$. The energy retention further exceeds the previously reported quasi-solid-state NICs.[16,17,64,73,74] NICs based on diffusion-limited electrodes deliver a poor specific power due to poor diffusion-limited ion kinetics in the high power region.

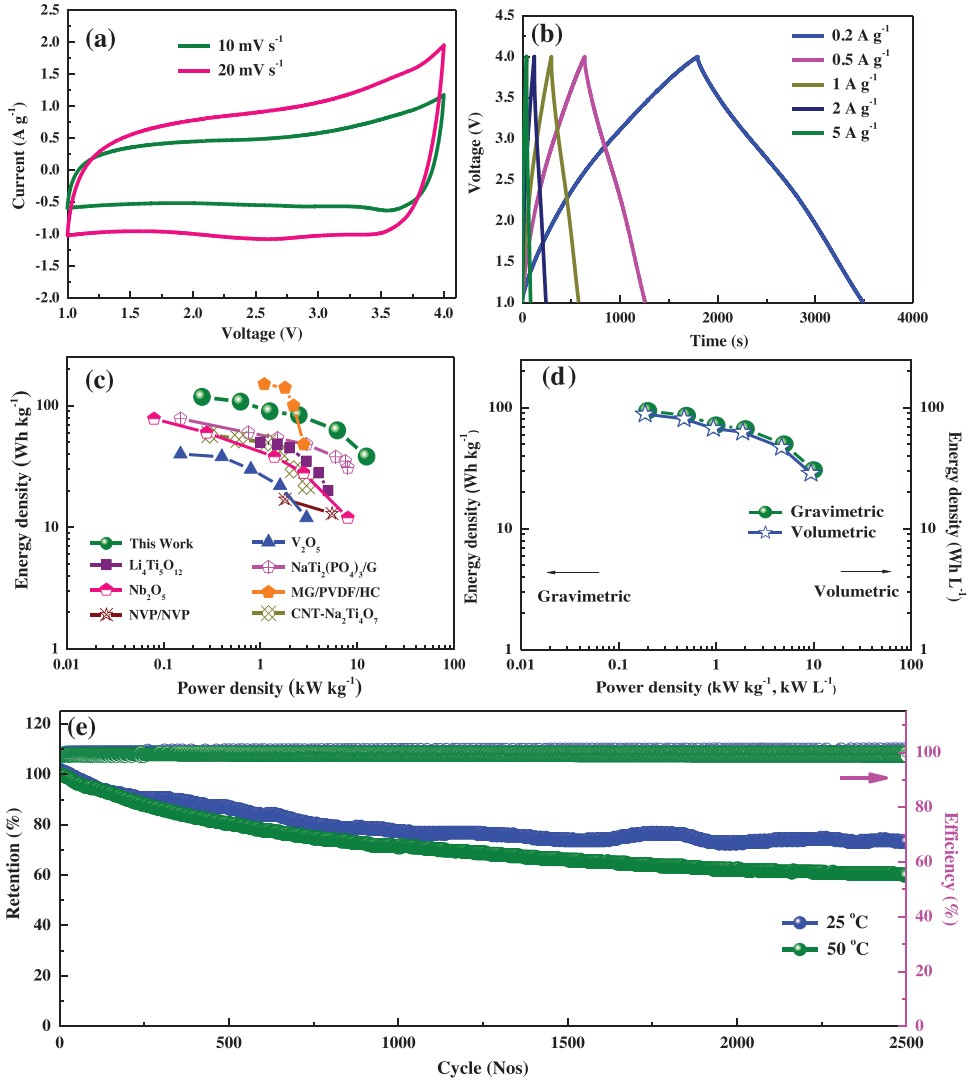

Figure 5. a) Cyclic voltammetry (CV) curves of the NIC at various scan rates, b) charge/discharge curves of the NIC, c) Ragone plot of the NIC and comparison with other systems, d) volumetric performance of NIC, and e) Cycling stability of the NIC.

However, higher power output has been achieved by storing the cations on the surface of the battery electrode even with a gel polymer type electrolyte. The P(VDF-HFP) membrane generally shows a lower interfacial resistance than conventional liquid electrolyte in glass fiber separator due to their high polarity and thereby easily buffers the fast movement of ClO_4 anions.[15]

Volumetric performance evaluation is important to realize their practical potential, and the volumetric performance is calculated from the densities of both electrodes and shown in Figure 5d. The quasi-solid-state capacitor delivered a high volumetric energy of ≈89 Wh L^{-1} at the volumetric power of 0.187 kW L^{-1}. This corresponds to gravimetric energy of ≈94 Wh kg^{-1} at 0.2 kW kg^{-1}, based on total mass of both the electrodes (including conductive carbon and binder). The quasi-solid-state NIC can reach a volumetric power of ≈9.4 kW L^{-1} while retaining an energy of ≈28.5 Wh L^{-1}. These values correspond to a gravimetric power of ≈10 kW kg^{-1} and an energy retention of ≈30.6 Wh kg^{-1} based on total mass on both the electrodes (including conductive carbon and binder). The optimized mass ratio between anode and cathode is 1:1 and increasing the mass ratio to 1:2 and 1:3 decreases the output energy of the system (Figure S9, Supporting Information) and it could be attributed to increase in diffusion resistance, and polarization of the electrodes with increased thickness.[75] Such a high volumetric performance cannot be achieved in NICs utilizing carbon-based and intercalation electrode. Additionally, the high amount of conductive carbon with other transition metal based battery electrode curtails the realization of high power–high energy NICs with high mass. Overcoming intercalation-type sodium storage with pseudocapacitive sodium storage enables a realization of high-performing NICs with high mass loading conditions. Table S2 (Supporting Information) compares the performance of several previously reported sodium and lithium-ion capacitors. It is clearly seen that the current NIC can perform extremely well even under high mass loading conditions and with a quasi-solid-state electrolyte. The most NICs achieve a high performance only at low

mass loading conditions (1–1.5 mg cm^{-2}). However, the current NIC delivers a superior energy and power output even under high mass loading (≈5 mg cm^{-2}).

The long-term cyclability of NICs is very crucial and determines the superiority of the system.[76–80] NICs showed a stability of ≈80% after 2500 cycles when tested at 3.5 A g^{-1} at room temperature (25 °C), while NICs showed a stability of ≈70% after 2500 cycles when tested at high temperature (50 °C) and both the NICs maintain a near ≈100% coulombic efficiency (Figure 5e). NICs developed with diffusion-limited intercalation compounds exhibit poor cyclability due to continuous active material deterioration and disadvantageous for developing a highly stable system. Unlike previous reports, where working potential window is greatly reduced to attain a high stability, compromising output energy, the present NIC achieved a high stability even with a large operating potential (1–4 V). The current performance advances NICs as a next-generation high energy–high power device, competing for a role in practical devices.

Such a high performance is attributed to (i) overcoming the diffusion-limited ion intercalation by surface-limited pseudocapacitance sodium-ion storage in TiO_2, (ii) highly conductive rGO bridges over nano-TiO_2 synergistically enhanced the electronic conductivity and Na-ion transfer kinetics even at high power, (iii) the low graphene content and nanostructured TiO_2 enables high mass loading in electrode and favors high volumetric capacity/energy, (iv) sandwiching the TiO_2 particles between graphene sheets protects the TiO_2 particles from large volume change during Na-ion adsorption, thereby maintaining the structural integrity of TiO_2 particles to achieve ultrahigh stability, (v) the large surface area of rGO-TiO_2 hybrids favorably enlarges the active surface area for Na-ion storage and the mesopore channels facilitate quicker Na-ion flow from the electrolyte for reaction at higher currents and high mass loadings, (vi) the polymer P(VDF-HFP) membrane synergistically allows the fast movement of ions toward both electrodes, and (vii) the fast pseudocapacitive kinetics is efficiently counterbalanced by mesoporous channels in RDC, greatly enhancing the ion transport for adsorption to achieve an improved rate performance.

4. Conclusion

In summary, we have demonstrated a new and simple approach to improve the performance of sodium-ion capacitors by utilizing pseudocapacitive sodium storage in TiO_2 and biomass-derived carbon. The efficient sodium storage kinetics of ultralow graphene-covered TiO_2 even under high mass loading conditions greatly addresses the volumetric issue in sodium-ion capacitors. The strategy of utilizing fast ion storage utilizing pseudocapacitance and adsorption holds great promise in achieving high energy at high power. Additionally, such a high energy–high power behavior is realized with a quasi-solid-state electrolyte, overcoming the safety issues with conventional liquid electrolyte. Importantly, high energy output achieved at high power along with high stability at room temperature and high temperature (50 °C) is far behind conventional ion capacitors and bridges performance gap between batteries and capacitors. The current research opens up new opportunities for highly safe NICs in next-generation high-energy, high-power applications that include electric vehicles and large-scale power grids.

5. Experimental Section

In a typical synthesis of rGO-TiO_2, the desired amount of GO solution was added to a mixture of water and ethanol and then heated to 80 °C with vigorous stirring. Another solution containing a diluted mixture of $Ti(O(CH_2)_3CH_3)_4$ and H_2SO_4 was mixed with the GO solution. The mixture was vigorously stirred for more than 12 h. The GO–TiO_2 hybrid formed was centrifuged and then reduced at 700 °C for 2 h in an Ar atmosphere.

For RDC, the waste watermelon rind obtained was initially dried at 120 °C for 48 h. The dried rind was precarbonized at 600 °C for 2 h in an Ar atmosphere. Later, the carbonized rind powders were activated by KOH at 800 °C for 1.5 h in Ar. The weight ratio of carbonized powder to KOH was maintained at 1:5. The obtained powder was grounded well and washed several times with 0.1 M HCl solution followed by distilled water to remove residual metal impurities.

The P(VDF-HFP) (M_w = 470 000, Kynar Flex 2801, Arkema) membrane was prepared by a solution-casting method. P(VDF-HFP) was dissolved into a mixture of acetone and distilled water at 30 °C for 12 h. The weight ratios of P(VDF-HFP), acetone, and water were 0.8, 8, and 0.4, respectively. The solution was then cast on a glass plate to allow evaporation of the acetone. After 1 h, it was immersed in methanol to allow pore formation and then dried at 80 °C, for 12 h in vacuum.

Supporting Information

Supporting Information is available from the Wiley Online Library or from the author.

Acknowledgements

This work was supported by the National Research Foundation of Korea (NRF) grant funded by the Korea government (Ministry of Science, ICT and Future Planning) (No. 2016R1A4A1012224).

Conflict of Interest

The authors declare no conflict of interest.

Keywords

batteries, graphene, porous carbon, quasi-solid-state, sodium-ion capacitors

Received: March 27, 2018
Revised: June 8, 2018
Published online: July 4, 2018

[1] M. Armand, J. M. Tarascon, *Nature* **2008**, *451*, 652.
[2] J. M. Tarascon, M. Armand, *Nature* **2001**, *414*, 359.
[3] P. Simon, Y. Gogotsi, *Nat. Mater.* **2008**, *7*, 845.
[4] S.-W. Kim, D.-H. Seo, X. Ma, G. Ceder, K. Kang, *Adv. Energy. Mater.* **2012**, *2*, 710.
[5] V. Palomares, M. Casas-Cabanas, E. Castillo-Martinez, M. H. Han, T. Rojo, *Energy Environ. Sci.* **2013**, *6*, 2312.

[6] H. Pan, Y.-S. Hu, L. Chen, *Energy Environ. Sci.* **2013**, *6*, 2338.
[7] J. Ding, H. Wang, Z. Li, K. Cui, D. Karpuzov, X. Tan, A. Kohandehghan, D. Mitlin, *Energy Environ. Sci.* **2015**, *8*, 941.
[8] R. Thangavel, K. Kaliyappan, D.-U. Kim, X. Sun, Y.-S. Lee, *Chem. Mater.* **2017**, *29*, 7122.
[9] S. J. Kim, M. Naguib, M. Zhao, C. Zhang, H.-T. Jung, M. W. Barsoum, Y. Gogotsi, *Electrochim. Acta* **2015**, *163*, 246.
[10] L. Hu, W. Chen, X. Xie, N. Liu, Y. Yang, H. Wu, Y. Yao, M. Pasta, H. N. Alshareef, Y. Cui, *ACS Nano* **2011**, *5*, 8904.
[11] C. Chen, Y. Zhang, Y. Li, J. Dai, J. Song, Y. Yao, Y. Gong, I. Kierzewski, J. Xie, L. Hu, *Energy Environ. Sci.* **2017**, *10*, 538.
[12] Y. Gogotsi, P. Simon, *Science* **2011**, *334*, 917.
[13] M. D. Stoller, R. S. Ruoff, *Energy Environ. Sci.* **2010**, *3*, 1294.
[14] F. Wang, C. Wang, Y. Zhao, Z. Liu, Z. Chang, L. Fu, Y. Zhu, Y. Wu, D. Zhao, *Small* **2016**, *12*, 6207.
[15] H. Li, L. Peng, Y. Zhu, X. Zhang, G. Yu, *Nano Lett.* **2016**, *16*, 5938.
[16] E. Lim, C. Jo, M. S. Kim, M.-H. Kim, J. Chun, H. Kim, J. Park, K. C. Roh, K. Kang, S. Yoon, J. Lee, *Adv. Funct. Mater.* **2016**, *26*, 3711.
[17] S. Dong, L. Shen, H. Li, G. Pang, H. Dou, X. Zhang, *Adv. Funct. Mater.* **2016**, *26*, 3703.
[18] F. Wang, X. Wang, Z. Chang, X. Wu, X. Liu, L. Fu, Y. Zhu, Y. Wu, W. Huang, *Adv. Mater.* **2015**, *27*, 6962.
[19] D. Xu, D. Chao, H. Wang, Y. Gong, R. Wang, B. He, X. Hu, H. J. Fan, *Adv. Energy Mater.* **2018**, 1702769.
[20] H. Kim, H. Kim, Z. Ding, M. H. Lee, K. Lim, G. Yoon, K. Kang, *Adv. Energy. Mater.* **2016**, 1600943.
[21] R. Wang, S. Wang, Y. Zhang, D. Jin, X. Tao, L. Zhang, *J. Mater. Chem. A* **2018**, *6*, 1017.
[22] C. Wang, F. Wang, Z. Liu, Y. Zhao, Y. Liu, Q. Yue, H. Zhu, Y. Deng, Y. Wu, D. Zhao, *Nano Energy* **2017**, *41*, 674.
[23] S. Liu, Z. Cai, J. Zhou, A. Pan, S. Liang, *J. Mater. Chem. A* **2016**, *4*, 18278.
[24] K. Kang, Y. S. Meng, J. Bréger, C. P. Grey, G. Ceder, *Science* **2006**, *311*, 977.
[25] Y. Wu, X. Liu, Z. Yang, L. Gu, Y. Yu, *Small* **2016**, *12*, 3522.
[26] D. Yang, J. Xu, X.-Z. Liao, Y.-S. He, H. Liu, Z.-F. Ma, *Chem. Commun.* **2014**, *50*, 13377.
[27] C. Chen, Y. Wen, X. Hu, X. Ji, M. Yan, L. Mai, P. Hu, B. Shan, Y. Huang, *Nat. Commun.* **2015**, *6*, 6929.
[28] V. Augustyn, J. Come, M. A. Lowe, J. W. Kim, P.-L. Taberna, S. H. Tolbert, H. D. Abruña, P. Simon, B. Dunn, *Nat. Mater.* **2013**, *12*, 518.
[29] Z. Jian, Y.-S. Hu, X. Ji, W. Chen, *Adv. Mater.* **2017**, 1601925.
[30] F. Cheng, J. Liang, Z. Tao, J. Chen, *Adv. Mater.* **2011**, *23*, 1695.
[31] G. Wang, L. Zhang, J. Zhang, *Chem. Soc. Rev.* **2012**, *41*, 797.
[32] H. Wang, C. Guan, X. Wang, H. J. Fan, *Small* **2015**, *11*, 1470.
[33] Y. Zhang, C. W. Foster, C. E. Banks, L. Shao, H. Hou, G. Zou, J. Chen, Z. Huang, X. Ji, *Adv. Mater.* **2016**, *28*, 9391.
[34] Y. Yeo, J.-W. Jung, K. Park, I.-D. Kim, *Sci. Rep.* **2015**, *5*, 13862.
[35] D. V. Bavykin, J. M. Friedrich, F. C. Walsh, *Adv. Mater.* **2006**, *18*, 2807.
[36] X. Rui, W. Sun, C. Wu, Y. Yu, Q. Yan, *Adv. Mater.* **2015**, *27*, 6670.
[37] S. Li, Y. Dong, L. Xu, X. Xu, L. He, L. Mai, *Adv. Mater.* **2014**, *26*, 3545.
[38] H. Wang, D. Mitlin, J. Ding, Z. Li, K. Cui, *J. Mater. Chem. A* **2016**, *4*, 5149.
[39] X.-Y. Shan, Y. Wang, D.-W. Wang, F. Li, H.-M. Cheng, *Adv. Energy Mater.* **2016**, *6*, 1502064.
[40] Y. Huang, J. Liang, Y. Chen, *Small* **2012**, *8*, 1805.
[41] A. Vu, X. Li, J. Phillips, A. Han, W. H. Smyrl, P. Bühlmann, A. Stein, *Chem. Mater.* **2013**, *25*, 4137.
[42] R. Thangavel, K. Kaliyappan, H. V. Ramasamy, X. Sun, Y. S. Lee, *ChemSusChem* **2017**, *10*, 2805.
[43] R. Thangavel, A. G. Kannan, R. Ponraj, V. Thangavel, D.-W. Kim, Y.-S. Lee, *J. Power Sources* **2018**, *383*, 102.
[44] G. Hasegawa, T. Deguchi, K. Kanamori, Y. Kobayashi, H. Kageyama, T. Abe, K. Nakanishi, *Chem. Mater.* **2015**, *27*, 4703.
[45] T. Yang, T. Qian, M. Wang, X. Shen, N. Xu, Z. Sun, C. Yan, *Adv. Mater.* **2016**, *28*, 539.
[46] F. Sun, H. Wu, X. Liu, F. Liu, H. Zhou, J. Gao, Y. Lu, *Nano Res.* **2016**, *9*, 3209.
[47] M. N. Tahir, B. Oschmann, D. Buchholz, X. Dou, I. Lieberwirth, M. Panthöfer, W. Tremel, R. Zentel, S. Passerini, *Adv. Energy. Mater.* **2016**, *6*, 1501489.
[48] L. Wu, D. Bresser, D. Buchholz, G. A. Giffin, C. R. Castro, A. Ochel, S. Passerini, *Adv. Energy. Mater.* **2015**, *5*, 1401142.
[49] X. Wang, L. Fan, D. Gong, J. Zhu, Q. Zhang, B. Lu, *Adv. Funct. Mater.* **2016**, *26*, 1104.
[50] R. Thangavel, A. S. Pandian, H. V. Ramasamy, Y.-S. Lee, *ACS Appl. Mater. Interfaces* **2017**, *9*, 40187.
[51] C. Wu, P. Kopold, Y.-L. Ding, P. A. van Aken, J. Maier, Y. Yu, *ACS Nano* **2015**, *9*, 6610.
[52] C. Zhang, B. Anasori, A. Seral-Ascaso, S.-H. Park, N. McEvoy, A. Shmeliov, G. S. Duesberg, J. N. Coleman, Y. Gogotsi, V. Nicolosi, *Adv. Mater.* **2017**, *29*, 1702678.
[53] M. Yu, J. Ma, M. Xie, H. Song, F. Tian, S. Xu, Y. Zhou, B. Li, D. Wu, H. Qiu, R. Wang, *Adv. Energy. Mater.* **2017**, *7*, 1602347.
[54] Q. Guo, Y. Ma, T. Chen, Q. Xia, M. Yang, H. Xia, Y. Yu, *ACS Nano* **2017**, *11*, 12658.
[55] J. R. Rani, R. Thangavel, S.-I. Oh, J. M. Woo, N. C. Das, S.-Y. Kim, Y.-S. Lee, J.-H. Jang, *ACS Appl. Mater. Interfaces* **2017**, *9*, 22398.
[56] H. He, Q. Gan, H. Wang, G.-L. Xu, X. Zhang, D. Huang, F. Fu, Y. Tang, K. Amine, M. Shao, *Nano Energy* **2018**, *44*, 217.
[57] L. Eliad, G. Salitra, A. Soffer, D. Aurbach, *J. Phys. Chem. B* **2001**, *105*, 6880.
[58] J. Ajuria, E. Redondo, M. Arnaiz, R. Mysyk, T. Rojo, E. Goikolea, *J. Power Sources* **2017**, *359*, 17.
[59] L. Zhao, *Adv. Mater.* **2010**, *22*, 5202.
[60] L. L. Zhang, X. S. Zhao, *Chem. Soc. Rev.* **2009**, *38*, 2520.
[61] J. Xu, Z. Tan, W. Zeng, G. Chen, S. Wu, Y. Zhao, K. Ni, Z. Tao, M. Ikram, H. Ji, Y. Zhu, *Adv. Mater.* **2016**, *28*, 5222.
[62] D. Chao, C. Zhu, P. Yang, X. Xia, J. Liu, J. Wang, X. Fan, S. V. Savilov, J. Lin, H. J. Fan, Z. X. Shen, *Nat. Commun.* **2016**, *7*, 12122.
[63] Y. Dai, Q. Li, S. Tan, Q. Wei, Y. Pan, X. Tian, K. Zhao, X. Xu, Q. An, L. Mai, Q. Zhang, *Nano Energy* **2017**, *40*, 73.
[64] Z. Chen, V. Augustyn, X. Jia, Q. Xiao, B. Dunn, Y. Lu, *ACS Nano* **2012**, *6*, 4319.
[65] T. Kim, G. Jung, S. Yoo, K. S. Suh, R. S. Ruoff, *ACS Nano* **2013**, *7*, 6899.
[66] R. Thangavel, K. Kaliyappan, K. Kang, X. Sun, Y.-S. Lee, *Adv. Energy Mater.* **2016**, *6*, 1502199.
[67] R. Thangavel, B. Moorthy, D. K. Kim, Y.-S. Lee, *Adv. Energy Mater.* **2017**, 1602654.
[68] Z. Le, F. Liu, P. Nie, X. Li, X. Liu, Z. Bian, G. Chen, H. B. Wu, Y. Lu, *ACS Nano* **2017**, *11*, 2952.
[69] H. Wang, C. Zhu, D. Chao, Q. Yan, H. J. Fan, *Adv. Mater.* **2017**, *29*, 1702093.
[70] Y. Ma, H. Chang, M. Zhang, Y. Chen, *Adv. Mater.* **2015**, *27*, 5296.
[71] C. Liu, Z. Yu, D. Neff, A. Zhamu, B. Z. Jang, *Nano Lett.* **2010**, *10*, 4863.
[72] H. Wang, Z. Xu, Z. Li, K. Cui, J. Ding, A. Kohandehghan, X. Tan, B. Zahiri, B. C. Olsen, C. M. B. Holt, D. Mitlin, *Nano Lett.* **2014**, *14*, 1987.
[73] H. Wang, D. Mitlin, J. Ding, Z. Li, K. Cui, *J. Mater. Chem. A* **2016**, *4*, 5149.
[74] H. Li, Y. Zhu, S. Dong, L. Shen, Z. Chen, X. Zhang, G. Yu, *Chem. Mater.* **2016**, *28*, 5753.

[75] S. Dsoke, B. Fuchs, E. Gucciardi, M. Wohlfahrt-Mehrens, *J. Power Sources* **2015**, *282*, 385.
[76] J. Yin, L. Qi, H. Wang, *ACS Appl. Mater. Interfaces* **2012**, *4*, 2762.
[77] S. S. M. Bhat, B. Babu, M. Feygenson, J. C. Neuefeind, M. M. Shaijumon, *ACS Appl. Mater. Interfaces* **2018**, *10*, 437.
[78] L.-F. Que, F.-D. Yu, K.-W. He, Z.-B. Wang, D.-M. Gu, *Chem. Mater.* **2017**, *29*, 9133.
[79] S. Liu, Z. Cai, J. Zhou, M. Zhu, A. Pan, S. Liang, *J. Mater. Chem. A* **2017**, *5*, 9169.
[80] S. Li, J. Chen, M. Cui, G. Cai, J. Wang, P. Cui, X. Gong, P. S. Lee, *Small* **2017**, *13*, 1602893.

